Applied Catalysis B: Environmental 148–149 (2014) 11–21

Contents lists available at ScienceDirect

Applied Catalysis B: Environmental

journal homepage: www.elsevier.com/locate/apcatb

Atomic layer deposition in the preparation of Bi-metallic, platinum-based catalysts for fuel cell applications

Emma Sairanen[a,*], Marta C. Figueiredo[b], Reetta Karinen[a], Annukka Santasalo-Aarnio[b], Hua Jiang[c], Jani Sainio[d], Tanja Kallio[b], Juha Lehtonen[a]

[a] Department of Biotechnology and Chemical Technology, Aalto University, P.O. Box 16100, FI-00076 Aalto, Finland
[b] Fuel Cell Research Group, Department of Chemistry, Aalto University, P.O. Box 16100, FI-00076 Aalto, Finland
[c] Department of Applied Physics, Aalto University School of Science, P.O. Box 15100, FI-00076 Aalto, Finland
[d] Department of Applied Physics, Aalto University School of Science, P.O. Box 11100, FI-00076 Aalto, Finland

ARTICLE INFO

Article history:
Received 3 July 2013
Received in revised form 10 October 2013
Accepted 22 October 2013
Available online 29 October 2013

Keywords:
Atomic layer deposition
Catalyst preparation
Direct methanol fuel cell
Methanol oxidation
Oxygen reduction reaction

ABSTRACT

Atomic layer deposition (ALD) is a thin layer synthesis method applied in this study for preparing carbon-supported mono-metallic Pt- and bi-metallic PtCo catalysts. The catalyst characterization confirmed that small metal particles with a narrow particle size distribution and high metal dispersion were obtained. The location of the metals on the surface was controlled by alternating the ALD cycles, and the formation of bi-metallic PtCo particles on the support was observed. The prepared catalysts proved to be active for methanol oxidation and oxygen reduction in an acidic media. In addition, the durability of the catalysts in electrochemical oxidation was enhanced by varying the metal cycle order in the catalyst preparation. After the deposition of Co on the catalyst, one ALD cycle of Pt favored the catalyst durability in the methanol oxidation reaction.

1. Introduction

Atomic layer deposition (ALD) is a solvent-free method for preparing catalysts by adding gaseous metal precursors to a solid surface. Under proper conditions, the metal precursors will attach themselves to the substrate surface by chemisorption and saturate it. This method has been widely used for preparing different thin films [1,2]; however, it can also be applied for catalyst preparation. ALD has been used to prepare catalysts with various supports, for example carbon-supported catalysts with metals like Pt [3], Pd [4,5], and Ru [6]. ALD has also been used for bi-metallic catalysts and thin films, for example to prepare Pt–Pd on Al_2O_3 [7], Ru–Pt thin films on SiO_2 [8], and Pt–Ir on SiO_2 [9]. ALD is an advantageous preparation method because it results in small metal particles with a narrow particle size distribution [4,5,10] and high metal dispersion [7] when compared to traditionally used impregnation methods. Moreover, ALD is especially interesting for bi-metallic catalysts because the availability of the metals on the catalyst surface can be controlled based on the order of the metal cycles in the ALD process.

Metal loading is one of the key parameters that define the activity of the supported heterogeneous metal catalysts. The loading can be controlled in various ways using different preparation methods. For example, with impregnation methods the metal loadings are controlled by the amount of metal precursor used [11], whereas with the ALD method they are controlled by precursor evaporation and surface temperature, by the number of precursor feed cycles, and by the surface sites on the catalyst support [12]. Another important feature of catalyst preparation is the metal crystal phase, which is typically controlled by the catalyst treatment performed after metal addition, like calcination or reduction. Reduction in particular is used to reduce the active metals to a metallic state on the catalysts [13]. Similar to the impregnation methods, with the ALD process different kinds of oxidation and reduction treatments after the precursor feed are used to remove ligands from the precursor and to obtain the desired metal oxidation state. Typically, an oxidation treatment with water, oxygen, or ozone is used most often in ALD to remove the ligands, especially in thin film applications [14]. ALD is a modification of chemical vapor deposition (CVD). The main difference between these methods is that in ALD the precursor reactions in gas phase are prevented by feeding the different precursors separately [14].

The properties of the catalyst—particle size, metal loading, metal distribution, and surface structure—play a key role in important electrocatalytic reactions, such as methanol oxidation (MOR) [15]

* Corresponding author. Tel.: +358 50 5300 324.
E-mail address: emma.sairanen@aalto.fi (E. Sairanen).

0926-3373/$ – see front matter © 2013 Elsevier B.V. All rights reserved.
http://dx.doi.org/10.1016/j.apcatb.2013.10.045

or oxygen reduction (ORR) [16]. These two reactions have been intensively studied due to their importance in fuel cell applications. The MOR is mostly studied on Pt-based catalysts [17] and the electrocatalytic oxidation of methanol on Pt is extremely dependent on such factors as surface crystallography [18,19] and particle size [20]. The desirable situation for highly efficient direct methanol fuel cell (DMFC) would be maximum methanol oxidation at low overpotentials. However, on Pt the strongly bonded CO intermediate hinders the MOR and causes a low current efficiency for CO_2 formation. A convenient way to modify the properties of the Pt catalyst and overcome this situation is to make alloys or bi-metallic surfaces [21]. Of the several bi-metallic catalysts that have been studied for methanol oxidation [22–24], researchers report that PtRu is the most active in terms of methanol oxidation. However, the high cost and limited supply of Ru has directed research in the direction of an alloying Pt with 3d transition metals, such as Co, Ni, and Fe. For the particular case of PtCo, the addition of Co promotes the onset potential of methanol dehydrogenation, thereby increasing the catalytic performance of the MOR compared to that of the mono-metallic Pt catalyst [25].

On the other hand, the cathode reaction in both polymer electrolyte fuel cells (PEFC) and DMFC is ORR. The kinetic limitations of this reaction lead to cell voltage losses, and developing new and better catalysts for this reaction would be a key way to improve PEFC. Considerable progress has been made on Pt-based, bi- and tri-metallic electrocatalysts, such as alloying Pt with 3d-transition metals, including Fe, Co, Ni [26], Cu [27], Cr [28], and Mn [29]. Of these catalysts, PtCo systems have received considerable attention because of their relatively high level of ORR activity and stability in acidic environments [30–32]. However, the reaction activity strongly depends on the ratios between the metals and the structure of the particles.

The aim of this paper was to study the ALD method for preparing carbon-supported, bi-metallic PtCo catalysts. Several catalyst batches were prepared in order to study the mechanism of bi-metallic particle formation on different metal loadings. Moreover, with the aim of increasing the stability of the PtCo catalysts, subsequent cycles of Pt were deposited on the initial PtCo catalyst. The physical characterization of the catalysts was performed by atomic emission spectroscopy (AES), X-ray diffraction (XRD), high-resolution transmission electron microscopy (HR-TEM), X-ray photoelectron spectroscopy (XPS), and CO chemisorption. Electrochemical characterization using cyclic voltammetry was also conducted to help physically characterize the ALD-prepared catalysts. Moreover, the catalytic activity for both MOR and ORR was evaluated.

2. Experimental

2.1. Catalyst preparation

The ALD catalyst preparation was carried out in a commercial, flow-type, F-120 ALD reactor (ASM Microchemistry) operating at a reduced pressure of 0.5–1 kPa. As a catalyst support material, commercial carbon black (Vulcan XC72R, Cabot GR-3875) was used as received with no further modifications. Before initiating the ALD precursor cycle, the support material was pretreated by drying in an N_2 flow (AGA, 99.999%) at 180 °C for 5 h. The metal precursors, the Pt precursor, platinum acetyl acetonate, $Pt(acac)_2$ (Volatec Oy), and the Co precursor, cobalt acetyl acetonate, $Co(acac)_3$ (Merck, 98%), were fed to the support with nitrogen as a carrier gas at 180 °C for 6 h at reduced pressure. An excess amount of precursor was used. Thereafter, the unreacted precursor was flushed from the reactor with nitrogen. The reaction cycles were alternated and repeated to achieve the desired metal loading. The abbreviations for the catalysts used in this paper represent the number and order of different precursor cycles, for example the Pt catalyst is a catalyst prepared using one Pt precursor cycle and the PtCo catalyst is prepared using one Pt precursor cycle followed by one Co precursor cycle. To obtain catalysts with different metal depositions, catalysts with varying precursor cycles were prepared sequentially by taking part of the initial catalyst from the reactor and adding metal cycles to the remaining part of it. To ensure the homogeneity of the catalyst, the batch sizes of the prepared catalyst were kept rather small; because of the amount of catalyst material needed for different characterizations, the prepared catalyst for all of the batches were not characterized after every cycle.

2.2. Physical characterization

The metal loadings on the ALD-prepared catalysts were determined by atomic emission spectroscopy (AES) (ICP-AES, Varian Liberty series II).

All of the studied catalysts were characterized by X-ray diffraction (XRD) (PanAnalytical X'Pert Pro). The XRD diffractograms were used to calculate the size of crystalline domains using the Scherrer equation (Eq. 1):

$$d = \frac{0.9\lambda}{\beta_{2\theta}\cos\theta}, \quad (1)$$

where d is the average crystalline domain diameter in nm, λ is the X-ray wavelength (Cu target 1.540 nm), θ is the Bragg angle in radians, and $\beta_{2\theta}$ is the full width at half maximum (FWHM) in radians. Crystalline domains are assumed to be monocrystals and the crystalline domain size d is discussed as the metal particle size in the article.

High-resolution transmission electron microscopy (HRTEM) was performed using a double-aberration-corrected JEOL 2200FS (JEOL) microscope equipped with a field emission gun (FEG) operating at 200 kV. The TEM was equipped with an energy dispersive X-ray (EDX) spectrometer for elemental analysis. A Gatan 4 k × 4 k UltraScan 4000 CCD camera was employed for digitally recording the HRTEM images. Gatan Digitalmicrograph software was used for camera control and image processing. The metal particle size was measured using the TEM images and the average metal particle sizes were calculated as arithmetic averages based on the measurements from the TEM images, assuming that those particles are of a spherical shape.

X-ray photoelectron spectroscopy (XPS) (SSX-100) was performed to measure the atomic surface concentration of metals and to analyze the metal oxidation states. The experiments were carried out using monochromatic AlKα X-rays and an electrostatic hemispherical analyzer. The spectra were recorded with a pass energy of 160 eV, a measurement area of 1 mm in diameter, and a step size of 0.05 eV. A high pass energy and large spot size were chosen to maximize the intensity level. For calculation of the surface concentrations, the platinum 4f, cobalt 2p, carbon 1s and oxygen 1s peaks were considered. The atomic concentrations obtained from XPS were converted into mass percentages for comparison with other methods. All of the binding energies were referenced to the carbon 1s peak at 284.5 eV.

CO chemisorption (Omnisorp 100CX) was performed to measure the active surface area of the catalysts as well as the particle size. In these standard procedure experiments, the catalysts were reduced 350 °C with hydrogen as a pretreatment before the CO chemisorption was performed at 30 °C. In the reduction, pure hydrogen (AGA, 99.999%) was fed through the sample and the pressure increased close to atmospheric pressure because of the flow. Before the CO chemisorption, the pressure was decreased to the vacuum and pulses of CO were fed. During the CO pulses, the pressure increased and the pressure increase was measured.

Table 1
Catalyst metal loadings and surface areas.

Catalyst		Pt	PtCo	PtCoPt	PtCoPtPt
Metal loading m-% determined by AES	Pt	13.97	13.78	8.06	20.53
	Co	0	1.38	0.79	0.79
Surface concentration m-% determined by XPS	Pt	13.9	13.2	18.8	34.0
	Co	0	2.8	2.9	1.5
Co:Pt ratio	Determined by AES		0.10	0.10	0.04
	Determined by EDS		0.11	0.06	0.04
Metal surface area, m^2/g (metal)		55	48	83	90

The average particle sizes were calculated assuming a CO/metal stoichiometry of 2 [33], and the spherical metal particles were calculated using Eq. (2) [34]:

$$d = \frac{6 \times M \times \rho_{site}}{D \times \rho_{metal} \times N} \quad (2)$$

where d is the average metal particle diameter in nm, M is the atomic mass (195.1 g/mol for Pt), ρ_{site} is the Pt surface site density (12.5 Pt atoms/nm^2), D is the metal dispersion on the surface, ρ_{metal} is the metal density (21.25 g/cm^3 for Pt), and N is the Avogadro constant.

The surface area of the metal particles was calculated using Eq. (3):

$$A = \frac{V_m \times N \times n \times A_{metal}}{V_{mol} \times C_{metal}} \quad (3)$$

where V_m is the adsorbed monolayer capacity in the chemisorption at m^3/g, A_{metal} is the surface area of the metal atom (8×10^{-20} m^2/Pt atom), V_{mol} is the ideal gas volume (22.4136×10^{-3} m^3/mol), and C_{metal} is the metal loading on the catalyst.

2.3. Electrochemical characterization

The electrochemical experiments were performed in a classical three electrode cell at a controlled temperature of 20 °C and under a nitrogen purge (AGA, 99.999%), with a potentiostat/galvanostat PGSTAT100 Autolab system and a rotating device from Pine Instruments. A Pt coil was used as a counter electrode and a reversible hydrogen electrode (RHE) as a reference electrode. The working electrode was prepared by depositing 4 μl of an ink (a mixture of 5 mg of a carbon-supported catalyst and 200 μl of ethanol carefully mixed with a magnetic stirrer and an ultrasonic bath) onto a glassy carbon electrode with a geometric area of 0.1963 cm^2. The glassy carbon support was previously cleaned by polishing it with an alumina solution and placing it in the ultrasonic bath. For the methanol oxidation and oxygen reduction experiments, 20 μl of a Nafion® solution (Aldrich, 5 m-%) was added to the ink in order to simulate the presence of ionomer in fuel cell conditions. All of the chemicals used were at least p.a. grade and deionized MQ water (Millipore, 0.04 μS/cm) was used for preparing the solutions.

The electrochemical characterization and cleaning of the carbon-supported catalysts was performed in a 0.5 M H_2SO_4 (Merck) solution at room temperature. Prior to use, all of the catalysts were cleaned via CO (AGA, 99.999%) adsorption and stripping. The active surface area of the catalysts was determined by the charge involved in the so-called hydrogen under potential deposition (UPD) region as well as by the CO oxidation charges.

The experiments performed for methanol oxidation were carried out in 0.5 M H_2SO_4 with 1 M of methanol (Merck). For the ORR, 0.1 M of $HClO_4$ (Merck) was used as an electrolyte, and O_2 (AGA, 99.999%) was purged through the solution until the saturation point was reached. During the experiments, the cell atmosphere was flushed with O_2 to maintain a constant concentration. The ORR results were analyzed using the Koutecky–Levich equation, where the total current, i, during oxygen reduction reaction consists of the diffusion part and the kinetic part, and it can be expressed as follows (Eq. 4):

$$\frac{1}{i} = \frac{1}{i_k} + \frac{1}{i_d}, \quad (4)$$

where i_d is the diffusion limited current owing to the mass transport and i_k is the kinetic current determined by the charge transfer.

For the rotating disc electrode (RDE) studies, the diffusion current is a function of the rotation speed, and it should obey the Levich equation (Eq. 5):

$$i_d = 0.62nFAC_{O_2}D_{O_2}^{2/3}\upsilon^{-1/6}\omega^{1/2}, \quad (5)$$

where n is the number of electrons transferred per one O_2 molecule, F is the Faraday's constant, A is the geometric electrode surface, C_{O_2} is the bulk oxygen concentration, D_{O_2} is the diffusion coefficient of oxygen, υ is the kinematic viscosity of the electrolyte, and ω is the electrode rotation speed. Under mass transfer limiting conditions, the Levich slope, B ($B = 0.62nFAC_{O_2}D_{O_2}^{2/3}\upsilon^{-1/6}$), is constant. Equations (4) and (5) establish a linear relationship between i^{-1} and $\omega^{1/2}$ with the y-intercept equaling the inverse of the kinetic current, i_k, and a slope proportional to the number of electrons exchanged for each oxygen molecule. By determining this slope, and by knowing the values of i^{-1} and $\omega^{1/2}$, it is possible to determine the number of electrons involved in the ORR.

3. Results

3.1. Physical catalyst characterization

Four different carbon supported catalysts were prepared with the ALD method: monometallic Pt and bi-metallic PtCo, PtCoPt, and PtCoPtPt where the order of the elements indicates the order in which the metals were introduced to the ALD reactor. The Pt and PtCo catalyst were from the same batch, however, due to the limitations of the batch size, PtCoPt and PtCoPtPt were form another batch. Several physical characterization methods were applied to determine the metal loadings, particle sizes, crystallographies, dispersions, and surface areas of the catalysts. Table 1 shows the catalyst metal loadings, the metal ratios, and the surface areas measured by CO chemisorption, Table 2 surface areas measured by hydrogen under potential deposition and CO oxidation, and Table 3 shows the metal particle sizes and dispersions.

Table 2
Comparison between the electrochemical active surface area values obtained from hydrogen under potential deposition (Hupd) and CO stripping. The values correspond to the electrodes prepared for the experiments from Figs. 5–9.

Catalyst	Electrochemical active surface area (cm^2)		Difference (%)
	Hupd	CO stripping	
Pt	0.817	0.799	−2.2
PtCo	0.106	0.108	+1.0
PtCoPt	0.523	0.516	−1.5
PtCoPtPt	0.550	0.560	+1.8

Table 3
Catalyst metal particle sizes and dispersion.

Catalyst		Pt	PtCo	PtCoPt	PtCoPtPt
Particle size (nm)	TEM	2.00	2.64	1.68	1.67
	CO chemisorption	2.54	2.90	1.68	1.56
	XRD (1 1 1)	1.71	1.92	1.51	1.56
	XRD (2 2 0)	1.90	1.91	1.73	1.88
Total metal dispersion (%)		45	39	68	73

The average sizes of the metal particles calculated based on the TEM, XRD, and chemisorption results were similar. In XPS measurements, Pt was mostly detected, indicating Pt being the dominant metal on the surface of catalysts. This validates the assumptions made in the calculation of CO chemisorption results using CO/Pt ratio of 2 and physical parameters for Pt. The metal surface areas and dispersions on the catalyst, calculated from the CO chemisorption, are presented in Tables 1 and 3. The metal dispersion and the available metal surface area measured by chemisorption (Tables 1 and 3) changed as a function of the average metal particle size; higher metal dispersions were logically obtained with smaller metal particles. In agreement with the chemisorption results the HRTEM images showed small metal particles evenly distributed throughout all the catalysts (see Fig. S1 in the supporting information for low-magnification images). The active surface areas measured by hydrogen under potential deposition and CO oxidation are presented in Table 2. Both values were quite similar (less than 2% difference and, for this reason, all of the results presented in this paper have been corrected for the value obtained from the H adsorption.

Fig. 1 shows particle size histograms of the catalysts, which were obtained by measuring diameters of 150–250 particles for each catalyst in the TEM images. The particle size distribution in the particle size histograms was narrow for all of the prepared catalysts. When comparing the particle sizes of the mono- and bi-metallic Pt and PtCo catalysts, we found that the addition of Co on Pt increased the particle size. The particle size distributions in the histograms shifted to larger particles from mono-metallic Pt and bi-metallic PtCo catalysts. When a new ALD Pt cycle is added to PtCoPt in order to obtain PtCoPtPt, there is a slight increase in the amount of larger particles, although the average particle size remains in the same range. The PtCo and PtCoPt samples are from a different catalyst batch, which might account for the difference between the histograms.

Aberration corrected HRTEM was employed to characterize the surface structure of the catalysts. This technology allows for atomic-resolution imaging and provides valuable information about the local topologies of active sites in the catalyst. Fig. 2 shows the HRTEM micrographs of the four catalysts prepared in this study. The representative images resemble a hexagonal shape for all of the catalysts consistent with the projection of ideal cuboctahedron. The diffraction patterns of the particles can be obtained using the Fourier Transform and information about the crystallographic plane of the particle edges can be obtained by matching the interplanar (inter-fringe) distances and the plane to plane angles. Lattice fringes with an inter-fringe distance of 2.26 Å and a plane-to-plane angle of 70° were found for the mono-metallic Pt catalyst. These values were quite close to those of the lattice spacing of the {1 1 1} planes in the bulk structure of the fcc Pt crystal. Moreover, lattice fringes of 1.96 Å, correspondent to {1 0 0} planes were also found. In summary, this projection shows, four {1 1 1} and two {1 0 0} facets placed on the edges of the hexagonal shape. Similar results were also obtained for the bimetallic PtCo, PtCoPt and PtCoPtPt (Fig. 2). However, different pattern for the PtCo catalyst in addition the one described previously was found. This latter pattern revealed lattice fringes with interplanar distances of 1.87, which are characteristic of {1 1 1} planes in bulk hpc Co.

XRD measurements were performed to study the crystal structure of the catalysts. The XRD diffractograms of all the ALD catalysts (Fig. 3) show wide peaks, indicating the small size of the particles. The peak intensity in the XRD diffractogram increased as a function of the metal loading. Four main peaks were observed in all the samples assigned to a face-centered-cubic (fcc) crystal phase. More detailed analysis shows peaks at 2θ positions—39.6°, 45.7°, 67.6°, and 81.5°—indicating a metallic Pt corresponding to (1 1 1), (2 0 0), (2 2 0), and (3 1 1) planes [35] (JCPDS card 01-087-0647), respectively (Fig. 3). The XRD reflection at 25° indicates the carbon support. The particle sizes calculated on the basis of the XRD results are presented in Table 3.

Based on the XPS results (Table 1), no significant changes in the Pt amount in the Pt and PtCo samples were detected. This is because of the low degree of Co loading compared to Pt loading.

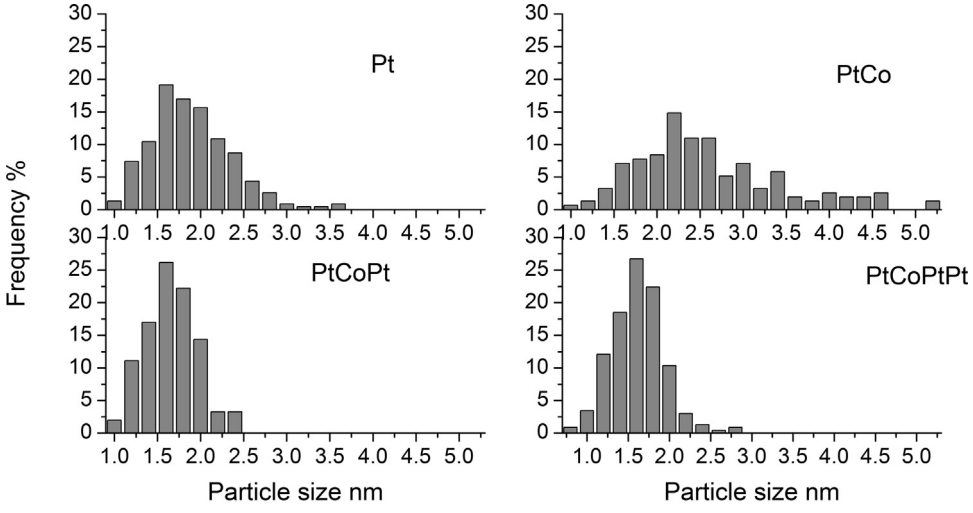

Fig. 1. Particle size histograms of ALD-prepared catalysts.

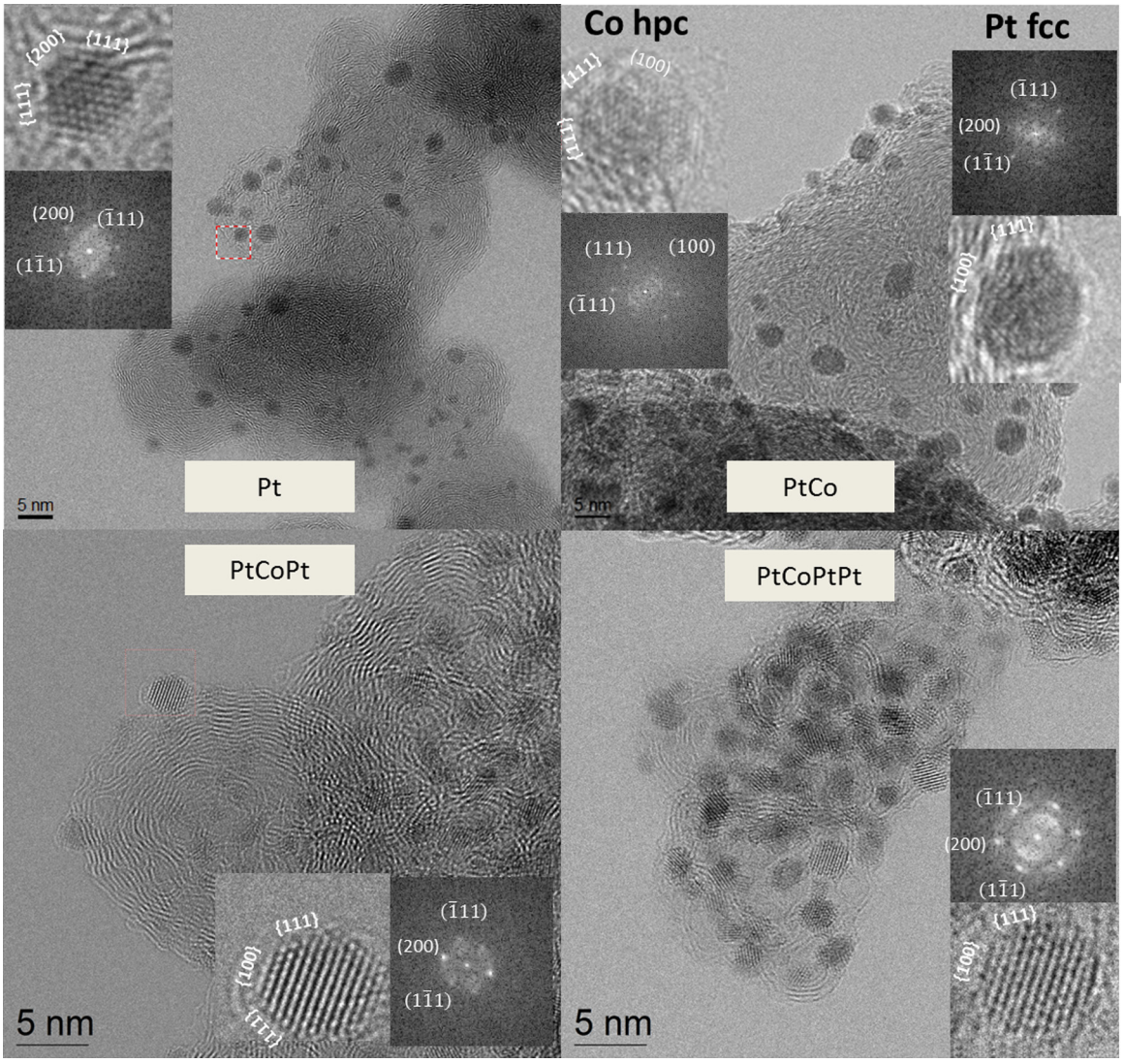

Fig. 2. TEM images of ALD-prepared catalysts.

Only metal loadings are given in Table 1 while the rest of the material is carbon from the support. Both the Pt and a small amount of Co were detected on the PtCo catalyst, which support the HRTEM findings that both the Pt and Co particles are present on the outermost surface of the catalyst. In general, no metals are detected in the XPS if they are not on the outermost surface of the catalyst. In the XPS, the Pt oxidation state was detected to be metallic in all of the samples, with a Pt $4f_{7/2}$ binding energy of roughly 71.5 eV. On the other hand, Co was found to be in an oxidized form, likely CoO or $Co(OH)_2$. This was evidenced by a Co $2p_{3/2}$ binding energy of approximately 781 eV and a satellite feature approximately 6 eV above the main peak, which is typical for high-spin Co^{2+} compounds [36].

Fig. 4a shows the catalyst particle size as a function of the catalyst metal loading. Fig. 4b shows the amount of Pt added to the catalyst per ALD cycle as a function of the metal loading of the catalyst before the cycle. Due to the limited size of prepared catalyst batches, measuring the metal loading for all the studied materials after every ALD cycle was not possible. Note that not all of the catalysts in Fig. 4b are reported in Table 1: the catalyst materials selected for electrochemical experiments were characterized more carefully. The amount of metal added on one ALD precursor cycle and the particle size of the catalyst metal depended on the catalyst metal loading.

The concentration values obtained by AES and XPS in Table 1 differ from each other in some cases. The metal loading measured using the AES technique is the metal loading in the bulk of the sample, whereas the concentration measured using the XPS technique is the metal content of the outermost 1–10 nm layer of the catalyst. Also, in XPS a homogenous composition is assumed to calculate the concentrations, even though the structure on a catalyst surface is clearly non-homogenous with surface enrichment of the active phases. For these reasons, the concentrations of Pt and Co according to XPS should be larger than from AES, if Pt and Co are found mainly on the surface. This appears to be the case, expect for the platinum content in the Pt and PtCo samples. For these samples, the particle sizes were, however found to be larger (Table 2) then for the PtCoPt and PtCoPtPt samples. The larger particle size could explain the discrepancy, since the Pt XPS signal depends on dispersion, with smaller dispersion corresponding to lower signal levels. For both the AES and XPS techniques, the metal amounts presented in Table 1 include the carbon support.

In EDX, metal loadings measured from separate regions of the catalyst surface were found to be similar indicating that metals are evenly dispersed on the surface as particles containing both metals and do not form mono-metallic particles on the surface. The Co:Pt ratio obtained from the EDX and AES results (Table 1) were either close to each other or almost identical. The Co:Pt ratio

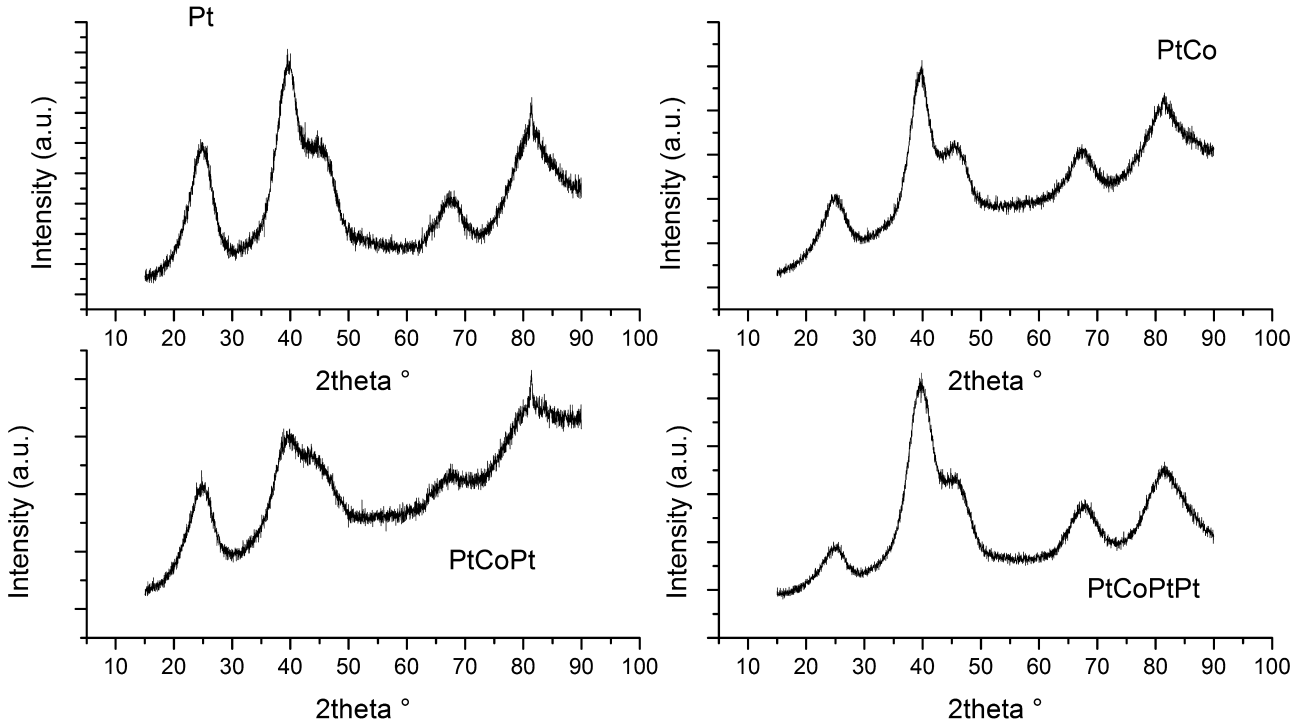

Fig. 3. X-ray diffractograms of ALD-prepared catalysts.

obtained from the AES and EDX measurements were in the same range. Fig. S2 in the supporting information shows an example of an EDX spectrum.

3.2. Electrochemical characterization

It is well known that the surfaces need to be clean before evaluating the real surface area of Pt-based catalysts because Pt is extremely active and sensitive to poisoning. Decontamination with CO has been widely used for cleaning the Pt surface [37–39] and bimetallic Pt catalysts [35,37] because its adsorption is strong and able to displace all expected contaminants from the surface. After completing the electrode preparation, first a cyclic voltammogram (CV) in 0.5 M H_2SO_4 was obtained to ensure that the preparation was successful. Later, CO was bubbled through the solution for three minutes and subsequently purged with N_2 for 20 min to remove all of the CO solution, the CVs for the CO oxidative stripping are presented in Fig. 5.

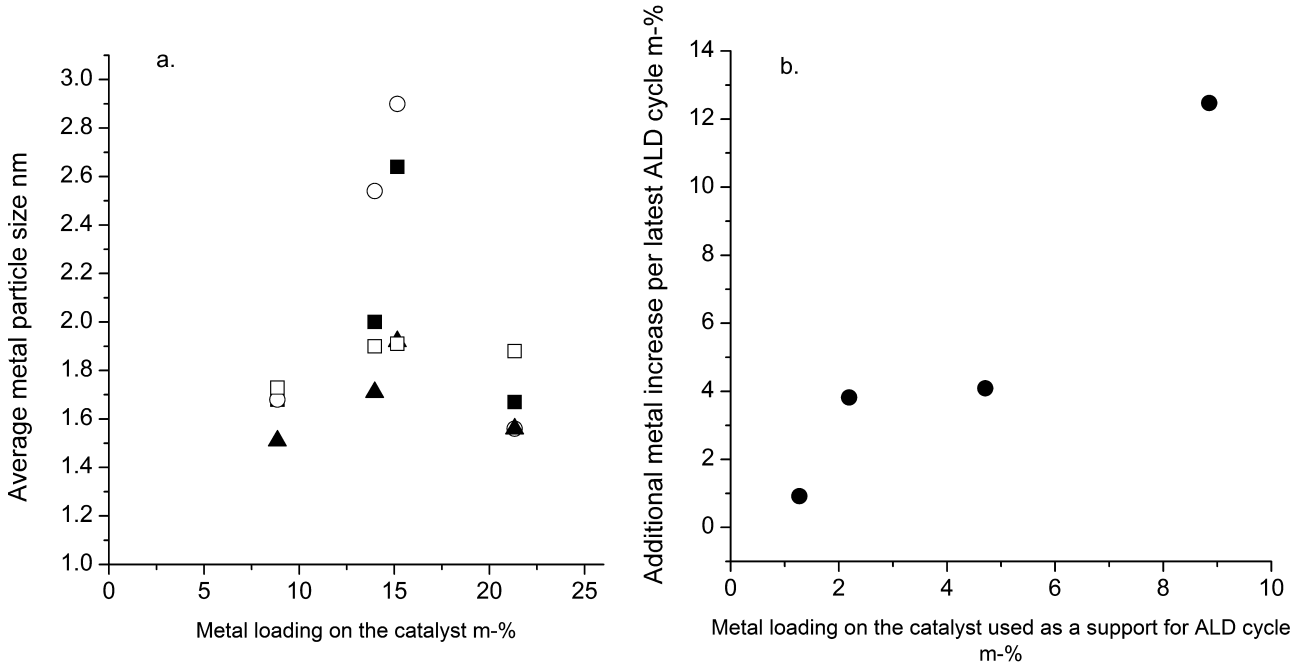

Fig. 4. (a) Catalyst particle size as a function of catalyst metal loading, particle size determined by TEM (■), CO chemisorption (○), XRD (1 1 1) (▲), and XRD (2 2 0) (□). (b) Metal loading added to one ALD cycle as a function of metal loading on the support before the cycle.

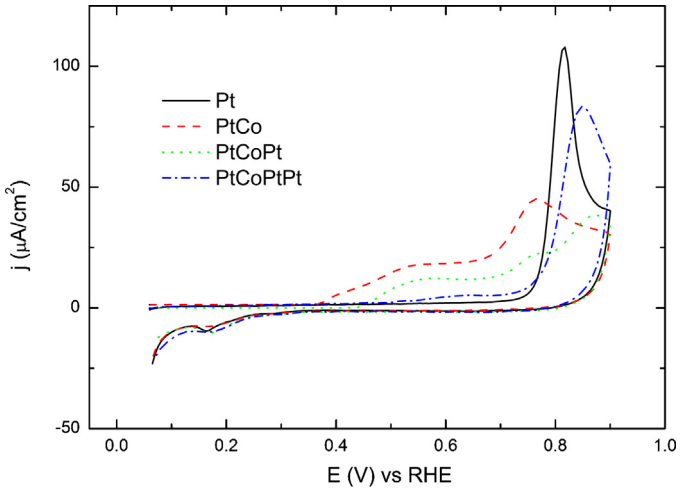

Fig. 5. CVs for CO stripping on the studied catalysts in 0.5 M of H_2SO_4, 10 mV/s.

As expected [40,41], the mono-metallic Pt catalyst did not show an oxidation current until potentials higher than 0.7 V, whereas finally a quite well-defined oxidation peak at 0.8 was observed. When the catalyst contains Co, the behavior is quite different. For PtCo, the onset potential of the CO oxidation clearly shifted to a lower potential at 0.4 V, at which point significant currents were already observed. Moreover, two peaks can clearly be distinguished at 0.53 and 0.76 V. When more Pt cycles were added to the PtCo catalyst, the CO stripping profile changed once again. The oxidation is described via three peaks on the PtCoPt sample. The first two were at the same potential (0.53 and 0.76 V) as those observed in the PtCo catalyst, whereas the third was at a higher potential: 0.88 V. The last cycle of Pt caused a decrease in the Co:Pt ratio on the PtCoPtPt catalyst and could be observed on the CO stripping at lower potentials (0.53 V) as a decrease in the oxidation currents (the peak is almost absent), and at high potentials (0.76 V) as an increase in the oxidation currents, together with a shift of this peak to higher potentials (when compared to a mono-metallic Pt catalyst).

Fig. 6 shows the voltammograms that correspond to the clean catalyst surfaces after CO stripping. The profiles obtained from the sulphuric acid look similar to both the mono-metallic and bi-metallic catalysts. Typically, currents resulting from H adsorption/desorption can be observed at potentials lower than 0.4 V for mono-metallic Pt catalysts. In this potential range, two features are evident at 0.16 and 0.27 V that correspond to the H adsorbed on the

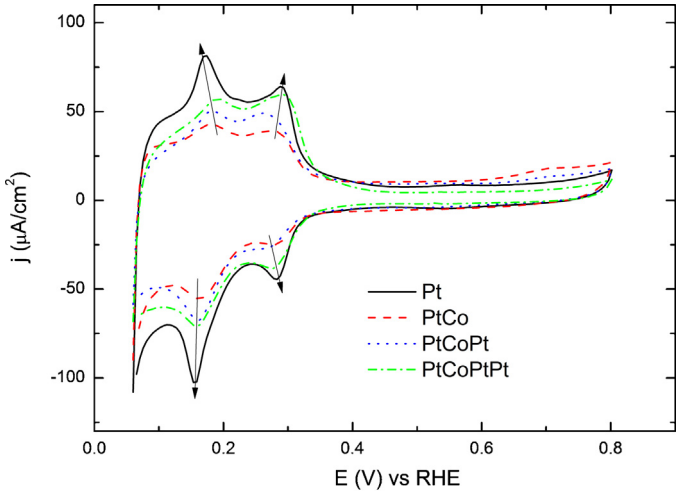

Fig. 6. Blank CVs of the catalysts in 0.5 M of H_2SO_4, 50 mV/s.

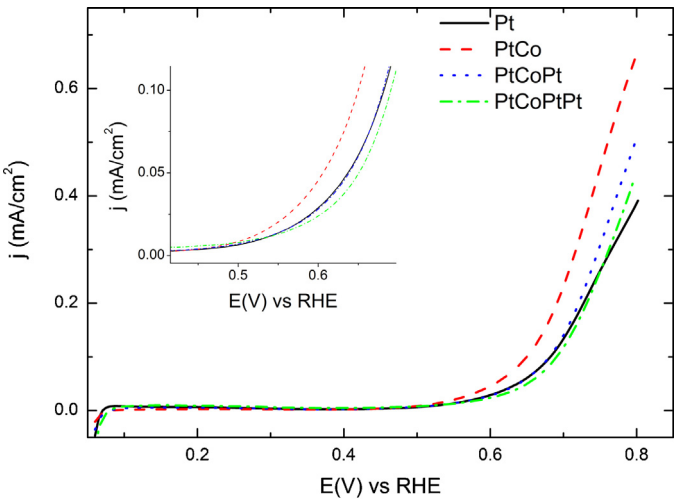

Fig. 7. Methanol oxidation CVs for the Pt, PtCo, PtCoPt and PtCoPtPt catalysts in 0.5 M of H_2SO_4 and 1 M of MeOH at 10 mV/s and 1800 rpm (inset figure: magnification of the onset potential region).

(1 1 0) and (1 1 1) domains, respectively [41]. This region is followed by a double layer at potentials higher than 0.4 V. These features were present for all of the catalysts studied. However, we noticed that the presence of Co decreased the definition of the H adsorption/desorption peaks at 0.16 and 0.27 V. Furthermore, a decrease in the Pt:Co ratio led to more pronounced features. Moreover, some oxidation currents at potentials higher than 0.6 V were evident on the PtCo catalyst.

3.3. Methanol oxidation reaction

In order to evaluate the catalytic activity of the ALD-prepared catalysts, the methanol oxidation reaction was studied. Fig. 7 shows the cyclic voltammetry curves of the Pt, PtCo, PtCoPt, and PtCoPtPt catalysts in 0.5 M of H_2SO_4 containing 1 M of methanol. The presence of Co increased the activity of methanol oxidation. When compared with mono-metallic Pt, the onset potential decreased by 50 mV and the current intensities were 1.5 times higher. These results are in good agreement with previous reports for PtCo catalysts [15,42,43]. The electrocatalytic behavior changes for the PtCoPt and PtCoPtPt catalysts. The PtCoPt catalyst still shows a higher level of activity than mono-metallic Pt; however, the onset potential for the reactions increased when compared with the PtCo surfaces. One fact that might affect the catalytic activity is the metal loading of the catalyst. On the other hand, the PtCoPtPt catalyst with a higher metal loading than the PtCoPtPt catalyst appeared to be less active in all potentials below 0.7 V. Moreover, the onset potential of PtCoPtPt is the highest of all four catalysts.

Surface poisoning is one of the main problems of using a Pt catalyst for methanol oxidation, and low degrees of poison formation are desirable since they contribute to a higher catalyst performance and life time. To evaluate the poisoning of the catalysts, we performed chronoamperometric experiments at 0.5 V for 900 s. In Fig. 8, it is possible to observe that the current densities of all the catalysts decay rapidly at the initial stage, which may be due to anion and water adsorption, the double-layer discharge, and the formation of intermediate species during methanol oxidation [42]. After approximately 100 s, the current decreased slowly at a constant rate. The methanol oxidation currents on the PtCo and PtCoPt were always higher than on the mono-metallic Pt nanoparticles, confirming that the electrocatalytic performance of PtCo catalyst is better than that of the Pt catalyst. As expected based on the

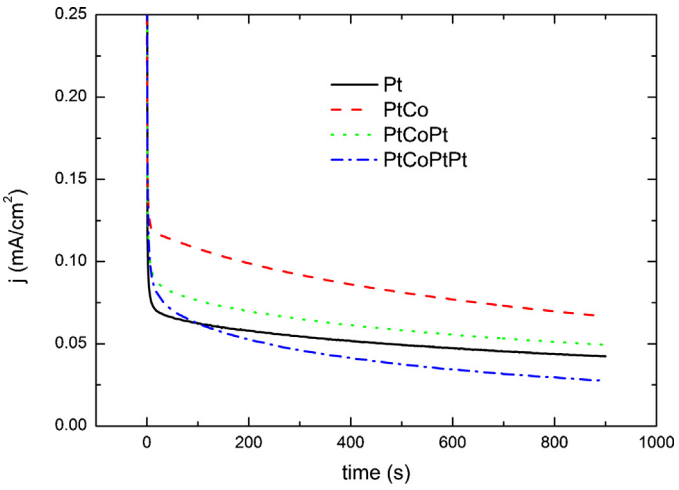

Fig. 8. Chronoamperometric curves for methanol oxidation (1 M methanol in 0.5 M of H_2SO_4) at Pt, PtCo, PtCoPt and PtCoPtPt surfaces, 0.5 V, 1800 rpm.

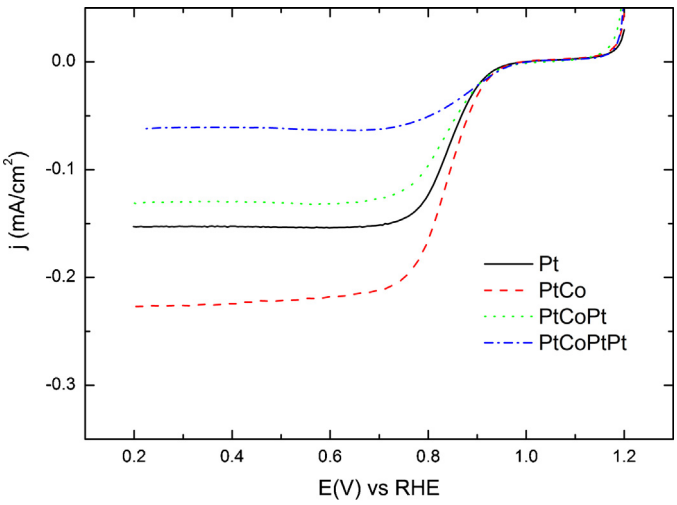

Fig. 10. ORR polarization curves for the Pt, PtCo, PtCoPt, PtCoPtPt catalysts in 0.1 M of $HClO_4$ saturated with oxygen, 5 mV/s and 1200 rpm.

cyclic voltammetry results, the current decrease occurs rapidly on the PtCoPtPt catalyst and is even more pronounced than on mono-metallic Pt, revealing a lower resistance to surface poisoning.

One of the most important issues that needs to be addressed before the commercialization of DMFCs is durability of electrocatalytic materials. To evaluate the electrochemical stabilities of the catalysts containing Co- and the advantages of subsequence Pt ALD cycles on the PtCo catalyst, cyclic voltammograms were measured for the MOR in 1 M of CH_3OH + 0.5 M H_2SO_4 at 10 mV/s for 1 h. Cyclic voltammetric (between 0.1 and 0.9 V vs RHE) was chosen rather than chronoamperometric experiments because the cycling will allow for oxidation on the surface poison products and a cleaner surface will thereby be obtained after each cycle. In this way, the effect of surface poisoning on the activity decrease is minimized. The maximum currents obtained for each cycle of the bi-metallic catalysts are presented in Fig. 9.

As shown previously for the methanol oxidation results (Figs. 7 and 8), the PtCo catalyst had higher currents throughout the whole time range, followed by the PtCoPt catalyst and finally the PtCoPtPt catalyst. The decrease from the first voltammetric cycle to the second was more pronounced with all of the catalysts. For the following cycles, the decrease was almost linear. To evaluate the durability of the catalyst, linear regressions were performed for the linear part of the curves. The slope represents the rate of deactivation of the catalysts and was taken as a measure of its durability. The PtCoPt catalyst exhibited the lowest slope (−3.8 mA/s), revealing the highest durability level among all the studied catalysts during the oxidation reaction. The degradation seems to be higher for both the PtCo (−4.9 mA/s) and PtCoPtPt (−4.2 mA/s) catalysts, and we did not observe any durability advantages for the PtCoPtPt catalyst during the last Pt deposition cycle.

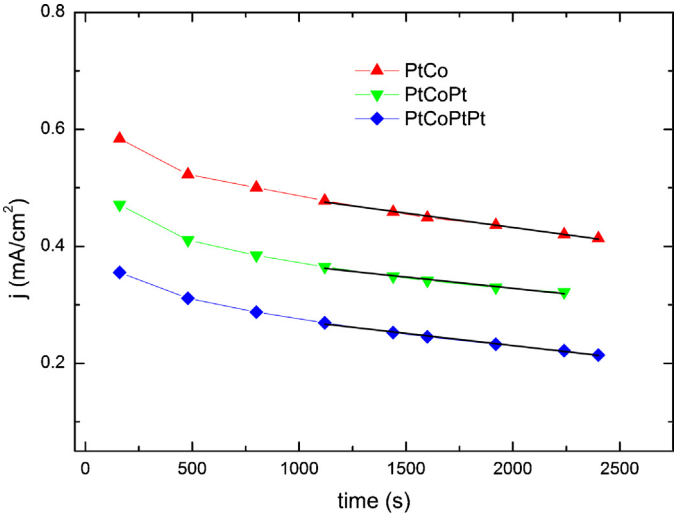

Fig. 9. Currents obtained at 0.8 V for the PtCo, PtCoPt, and PtCoPtPt catalysts as a function of cycle time.

3.4. Oxygen reduction reaction

Fig. 10 shows the ORR polarization curves for the ALD-prepared catalysts at 1200 rotations per minute (rpm) in 0.1 M of $HClO_4$ saturated with O_2. The onset potential of the ORR had clearly shifted towards more positive potentials for the PtCo sample containing more Co on the outermost surface. Moreover, not only did the onset potential in the ORR shift towards more positive potentials, but the performance of the PtCo catalyst shifted towards them throughout the polarization range as well; this was clearly superior compared to the rest of the studied catalysts. Additionally, the PtCo catalyst had a much larger limiting current (i_L). However, the activity for oxygen reduction was lower on the bi-metallic PtCoPt and PtCoPtPt catalysts than for mono-metallic Pt. These types of curves demonstrate three different regions of interest. For all the samples, the kinetic control region lay between 0.9 and 0.75 V, whereas the mixed control region lay between 0.75 and 0.45 V and the diffusion limited region lay between 0.45 and 0.2 V where perfectly defined plateau can be observed [44].

The results obtained from the polarization curves were studied using the Koutecki–Levich analysis described previously in the experimental part of the paper (Section 2.4). The number of electrons involved in the reactions was calculated using Eqs. (4) and (5) and the results are presented in Fig. 11. Oxygen can either be reduced to water consuming four electrons per one O_2 molecule, or to hydrogen peroxide consuming two electrons per one O_2 molecule. Pt promotes the transfer process for the four electrons, while the ORR catalyzed by PtCo proceeds through a mixed mechanism. With additional Pt cycles, the number of electrons involved approaches four, suggesting a behavior more similar to mono-metallic Pt. The shift of the reaction mechanism towards a higher production of peroxide was previously reported for PtCo [45] and Co [46] catalysts.

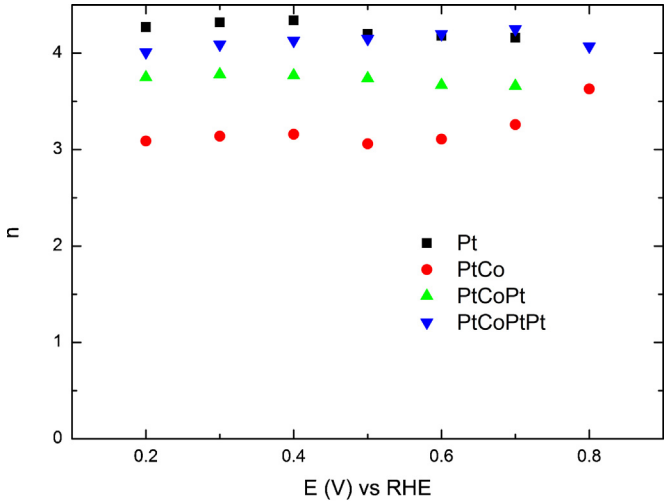

Fig. 11. Number of electrons involved in ORR on the Pt, PtCo, PtCoPt, and PtCoPtPt catalysts at different potentials.

4. Discussion

Mono-metallic Pt and bi-metallic PtCo catalysts prepared with a different number of precursor feed cycles were studied. The increase in the metal content of the sample per one ALD cycle is very strongly dependent on the metal content of the sample before the cycle. The more metal there already is on the catalyst, the more was observed to be attached per next cycle, as illustrated in Fig. 4. In addition, this trend was observed to increase linearly as a function of the metal content of the catalyst. Varying Co:Pt ratios on the catalyst did not change this trend. This indicated that the metal particles grow on top of the existing metal particles, and in addition, some new particles emerge as can be seen in histograms (Fig. 1). There are three primary thin-film growth modes: a layer-by-layer mode (also known as the Frank-van der Merve mode), an island mode (also known as the Vollmer–Weber mode), and a layer-plus-island mode (also known as the Stranski–Krastanov mode) [47]. These modes can also be applied for ALD growth. Depending on the mode, the metal atoms are either more strongly bound to the catalyst support surface sites or to the other metal particles. In the layer-by-layer mode, completed layers are formed and the next layer starts to grow after the previous one is complete; also, the metal is more strongly bound to the support than to the other metal atoms. In the island growth mode, metal nucleates and forms particles instead of monolayers because metal atoms bond more strongly to other metal atoms than to the support. When using a combination of these two modes, the layer-plus-island growth mode, a completed layer of metal first forms on the support surface, after which metal islands form on the metal layer [35]. All of these growth modes are possible in thin-film applications, such as for ALD growth on glass surfaces. When applying the ALD method to porous supports, like in a catalyst preparation, the growth mainly follows the island growth mechanism [48]. The results for different metal loadings supported the island growth theory [48], in which metals deposited on successive ALD precursor cycles attach more strongly to metal sites than to the support surface sites. The results also demonstrate that this was the case for the dependency of metal loading on one ALD cycle in relation to the amount of metal in the catalyst (Fig. 4). The existing literature shows that the surface sites of carbon black, which we also used in this study, mainly consist of carboxylic acid and quinone groups [49].

When comparing the particle sizes of the mono- and bi-metallic Pt and PtCo catalysts, we found that the addition of Co on Pt increased the particle size. In the particle size histograms, the proportion of smaller particles decreased while the proportion of larger metal particles increased from a mono-metallic to bi-metallic catalyst, indicating that part of the added Co had attached on or next to the small Pt particles instead of on the catalyst support surface; as a result, they formed larger bi-metallic particles. However, mono-metallic Co particles were also detected in the HR-TEM images of the PtCo catalyst, indicating that Co forms both mono- and bi-metallic particles on the support. When comparing the Pt:Co ratios of the m-% determined when using AES (Table 1), as well as the changes in the particle size distribution between the Pt and PtCo samples, the Co loading was too small to explain the increase in the particle sizes. That is why the increase in the particle size might also be partly related to the growth of the Pt particles via the agglomeration of small Pt particles to larger ones.

The last Pt cycle added to the PtCoPt catalyst to obtain the PtCoPtPt catalyst did not increase the average particle size (Table 3). Instead, when comparing these samples, the particle size distribution in the TEM histograms shifted towards the smaller particles, and at the same time, a small increase in the amount of larger particles was observed for the two samples. According to the XPS results, the Co atomic surface concentration decreased from the PtCoPt to the PtCoPtPt catalyst even though the Co loading did not change. This might indicate that Pt attaches partly on top of the Co on catalysts, which was seen as a weakened XPS signal of Co. If the Pt only attaches to the PtCo particles, the particle size will increase and the particle size distribution will shift towards larger metal particles, as was the case with the Pt and PtCo catalysts. Based on these results, we conclude that Pt both attaches to the PtCo particles and forms new Pt particles on the support. Metal particle sizes as a function of metal loading (Fig. 4) exhibited a maximum metal loading at 15 m-% of Pt (PtCoPt catalyst), after which the average particle size decreased (on PtCoPtPt catalyst). This suggests that new mono-metallic Pt particles formed rather than attaching Pt particles to the PtCo particles on the surface on PtCoPt and PtCoPtPt catalysts. Because only a small number of larger particles formed in the PtCoPt and PtCoPtPt samples, the possible clustering of Pt considered in the case of mono- and bi-metallic catalysts is thought to be insignificant in these samples. This would indicate that the stabilization effect of the Co affecting the bi-metallic catalysts would prevent the Pt particles from clustering on the surface.

For the mono-metallic Pt and the bi-metallic PtCo samples, the metal surface area and dispersion decreased because larger particles formed on the bi-metallic catalyst, which resulted in lower surface area. For the PtCoPt and PtCoPtPt catalysts, the metal dispersion and metal surface area increased when more metal was added to the surface, and consequently, the metal particle size was lower than with the Pt or PtCo catalysts. This result supported the analysis done based on the metal loadings and particle sizes, suggesting that the last added cycle of Pt formed some new metal particles on the surface rather than becoming attached to the PtCo particles or close to them.

Metal crystallography was analyzed by XRD (Fig. 3) and HR-TEM (Fig. 2). With XRD, metallic Pt with a face-centered-cubic (fcc) crystal phase was detected. From the different Pt reflections in the diffractograms (Fig. 3), we detected the Pt (1 1 1) and Pt (2 2 0) reflections most clearly. Co reflections were not detected in XRD; Hernández-Fernández et al. [50] have suggested that Co is not detected in bi-metallic PtCo samples because the particles are either nanosized or amorphous, which XRD cannot detect. The possible formation of alloys was detected in the bi-metallic PtCo catalysts when using XRD because the reflections shifted to higher detection angles [35]. In the case of ALD-prepared catalysts this shift was not seen suggesting that Pt and Co form bi-metallic nanoparticles instead of alloys. This observation was also supported by the lattice parameter calculated based on the XRD diffractograms, which was 3.9 nm (characteristic of Pt bulk) for all the

catalysts. The XRD peaks are typically wide for small particles [50], which was also observed in the diffractograms (Fig. 3) for the ALD-prepared catalysts. The metal oxidation state results analyzed using XRD and XPS measurements supported one another. In the XRD measurements, we detected metallic Pt and Pt in the all the samples was also metallic in the XPS measurements. On the basis of the XPS results, Co was an oxide, likely CoO or $Co(OH)_2$. Co oxidation state based on the XRD results could not be determined. The metal oxidation state in ALD deposition is controlled by the gas treatment after the precursor feed, with air typically being used in various thin film applications. In this study, the aim was to prepare metallic Pt particles; that is why N_2 was chosen as a treatment gas after the precursor feed instead of gases containing oxygen.

The analysis of the high-magnification HRTEM images showed that the metal particles in all the catalysts have a well-defined shape, suggesting a high ordering of the atoms on the surface. Thus, the particles can be considered individual nanocrystals. Another important result was that mono-metallic Co particles with hcp structure in the PtCo catalyst were observed. This observation indicates that Co is not only deposited on Pt, but that it is also directly deposited on the carbon support, thereby forming mono-metallic Co particles. This fact is also corroborated by the wider particle size distribution observed in the particle size histograms of the PtCo catalyst. The average particle size increased due to Co deposition on the Pt particles; however, we also observed smaller and probably new Co particles. Nevertheless, it should be kept in mind that the activity of the PtCo catalyst is still better than that of the other catalysts for the MOR and ORR reactions studied in this work.

The crystalline characteristics of the particles could also be observed in the electrochemical characterization (Fig. 6 and Table S1 in the supporting information). The mono-metallic Pt catalyst showed well-defined peaks for H adsorption (Fig. 6) at 0.16 and 0.27 V, which is related to the (1 1 0) and (1 0 0) sites on the particles. This finding was to be expected based on the crystalline structure observed in the HRTEM images (Fig. 2) [38]. These peaks became smoother when Co was added, and subsequent additions of Pt to the PtCo catalyst in the ALD synthesis contributed to a behavior more similar to that of Pt in this potential region. We expected that there would be differences on the double layer regions of the blank CV measurements (Fig. 6) as a consequence of the different metal loadings on the catalysts. They will present different metal/carbon ratios because the lower metal loadings will have a higher amount of carbon on the sample, resulting in higher double layer currents [38].

Fig. 7 shows that on the PtCo catalyst, the onset potential of the CO oxidation shifted to a much lower potential compared to the Pt. These results suggest the dramatic diminution in the affinity of CO in Pt when Co is present in the catalyst. This is due to the decrease in the interaction between CO and Pt caused by the lowering of the d-band center [51–53]. Nevertheless, the enhancement of the CO oxidation on the bi-metallic catalyst can also be ascribed to a bi-functional mechanism where the early oxidation of Co provides the oxygen needed for the reaction to occur [54]. For the catalyst where cycles of Pt were added to the PtCo (i.e. PtCoPt and PtCoPtPt), the behavior changed and became more similar to Pt because an increase in the Pt loading decreases the Pt:Co ratio and part of Co particles were covered by Pt.

The study of the catalysts in methanol oxidation showed that the activity increases with the presence of Co. When compared with mono-metallic Pt, the onset potential decreased by 50 mV and the current intensities are 1.5 times higher. These results are in good agreement with previous reports regarding PtCo surfaces [15,42,43]. As mentioned above and demonstrated by the results obtained from CO stripping, the CO adsorption rate for the bi-metallic PtCo particles is slower on mono-metallic Pt, which can be attributed to the electronic effect of Co on Pt. The decrease in the CO adsorption energy is due to the shift of the d-band center; meanwhile, the presence of Co oxides also provides an oxygen source for CO oxidation at lower potentials based on the bi-functional mechanism. The bi-functional mechanism will cause the earlier oxidation of CO, thereby enhancing the methanol oxidation rate. The onset potential of the PtCoPtPt catalyst was the highest of the four catalysts studied, suggesting that the Pt:Co ratio of this catalyst was probably too low for the methanol oxidation to occur.

It has been reported [55] that particles with low Co loading (Pt:Co > 1:1) outperform those with a high Co loading (Pt:Co < 1:1) and that the optimum Pt:Co ratio is about 1:0.5 for the best electrocatalytic activity. It should be noted that the present catalysts had much lower ratios—1:0.1—for both the PtCo and PtCoPt catalysts and 1:0.04 for the PtCoPtPt catalyst. In addition, with the exception of the PtCoPtPt catalyst, the metal loadings were smaller than the loadings of commercially available Pt. Still, we noticed remarkable improvements in the catalytic effects. The metal particle size of the catalyst plays an important role in electrocatalysis. For methanol oxidation, it has been observed that a decrease in the size of the nanoparticles causes a decrease in the reactivity with Pt nanoparticles in the size range from 1.2 to 4.5 nm. For this reason, the lower activity of the PtCoPt catalyst with a particle size of 1.6 nm compared to PtCo with a particle size of 2.6 nm with similar Pt:Co ratios and even of Pt with a particle size of 2.0 nm can also be due to the smaller particle sizes.

The durability data (Fig. 9) showed that although the catalytic activity effect decreased when we added a new cycle of Pt, the catalyst's durability increased. This is an extremely important result for fuel cell applications, where the durability of the catalysts has been one of the biggest problems hindering commercialization. Even with lower performances in fuel cells, more durable catalysts have many advantages. On other hand, the last cycle of Pt on the PtCoPtPt catalyst did not increase the durability of the catalyst because the stability of the catalyst became quite similar to the Pt particles and the activity was lower. This effect can be explained by taking into account the fact that when new mono-metallic Pt particles were formed, the proportion of bi-metallic PtCo particles decreased. Of the catalysts studied in this work, bi-metallic metal particles were more active than mono-metallic particles. That is why the decreasing proportion of bi-metallic particles resulted in decreasing activity; moreover, smaller particles will be less stable.

Another model reaction used to test the catalysts prepared by the ALD method was oxygen reduction reaction (ORR). As reported previously, for PtCo catalysts ([44] and the references therein) the presence of Co increases the catalytic activity in the direction of ORR due to a decrease in the oxygen binding energy on the bi-metallic catalyst surface. The ALD-prepared PtCo demonstrated this effect perfectly compared with the mono-metallic Pt (Fig. 10). With this catalyst, the number of electrons involved in the ORR process suggested a mixed mechanism, which displaced the ORR reaction in favor of hydrogen peroxide production. This reaction is an undesirable side reaction in fuel cell applications because it reduces the cell's efficiency. However, the $2e^-$ reduction of O_2 to hydrogen peroxide makes it possible to synthesize peroxide by electrochemical means. This is also possible for other applications in addition to fuel cell applications with these types of catalysts.

For the catalysts with Pt cycles after the Co, the ORR activity decreased; this contradicted the expected behavior. This can be explained by the metal particle size effect. Oxygen reduction is very sensitive to the size of the catalyst particle. It has been shown [56] that the oxygen reduction activities in $HClO_4$ solutions on the Pt particles with a particle diameter range of 1–5 nm and increases twofold from 1.3 to 2.2 nm and decrease as the particle size further increases. The particle sizes between the PtCo (2.63 nm), Pt (2.0 nm), and PtCoPt catalysts as well as the PtCoPtPt (1.6 nm) catalyst were in a size range where small differences in the particle size

will represent significant differences in catalytic activity. Nevertheless, this study has shown that ALD is a good and clean method for preparing bi-metallic catalysts for fuel cell applications.

5. Conclusions

Carbon-supported mono-metallic Pt catalysts and bi-metallic PtCo catalysts with high dispersion and narrow particle size distributions were prepared using the ALD method. Using the ALD method, we demonstrated that the number and order of the precursor cycles have an effect on the metal particle size and the availability of the metals on the catalyst support. A similar Pt crystallography in all of the prepared samples was observed. The prepared catalysts proved to be active for two important reactions in fuel cell applications: methanol oxidation and oxygen reductions. With bi-metallic PtCo particles higher methanol oxidation activity and lower onset potential than with mono-metallic Pt particles was observed. We also studied the effect of the precursor cycle number in the catalyst preparation on electrochemical activity. Additional Pt cycles in the catalyst preparation decreased the catalyst activity because the Co particles were partly covered with Pt, and the Pt:Co ratio decreased. On the other hand, the durability of the catalyst increased. In this study, the ALD method was used to prepare bi-metallic, PtCo-containing catalysts with high levels of catalytic activity. Even though the cobalt loading in bi-metallic samples was small, the clear difference between mono- and bi-metallic catalysts was observed. This method proved to be very promising and was quite suitable for synthesizing a stable and active bi-metallic, carbon-supported catalyst with a controlled crystalline structure for electrochemical oxidation reactions.

Acknowledgments

Heidi Meriö-Talvio is acknowledged for carrying out the chemisorption measurements. The CNB-E project, which is part of the Multidisciplinary Institute of Digitalization and Energy (MIDE) program, is acknowledged for its financial support. The authors acknowledge the Laboratory of Inorganic Chemistry at Aalto University for providing us with access to X-ray diffraction equipment and Mr. Matti Lehtimäki for his assistance with the measurements. Marta C. Figueiredo and Tanja Kallio acknowledge financial support from Aalto University.

Appendix A. Supplementary data

Supplementary data associated with this article can be found, in the online version, at http://dx.doi.org/10.1016/j.apcatb.2013.10.045.

References

[1] T. Suntola, Mater. Sci. Rep. 4 (1989) 261–312.
[2] E.-L. Lakomaa, Appl. Surf. Sci. 75 (1994) 185–196.
[3] C. Liu, C.-C. Wang, C.-C. Kei, Y.-C. Hsueh, T.-P. Perng, Small 5 (2009) 1535–1538.
[4] E. Sairanen, R. Karinen, M. Borghei, E.I. Kauppinen, J. Lehtonen, ChemCatChem 4 (2012) 2055–2061.
[5] E. Rikkinen, A. Santasalo-Aarnio, S. Airaksinen, M. Borghei, V. Viitanen, J. Sainio, E. Kauppinen, T. Kallio, A.O.I. Krause, J. Phys. Chem. C 115 (2011) 23067–23073.
[6] A.J. Plomp, H. Vuori, A.O.I. Krause, K.P. de Jong, J.H. Bitter, Appl. Catal. A: Gen. 351 (2008) 9–15.
[7] Y. Lei, B. Liu, J. Lu, R.J. Lobo-Lapidus, T. Wu, H. Feng, X. Xia, A.U. Mane, J.A. Libera, J.P. Greeley, J.T. Miller, J.W. Elam, Chem. Mater. 24 (2012) 3525–3533.
[8] S.T. Christensen, H. Feng, J.L. Libera, J. Guo, J.T. Miller, P.C. Stair, J.W. Elam, Nano Lett. 10 (2010) 3047–3051.
[9] S.T. Christensen, J.W. Elam, Chem. Mater. 22 (2010) 2517–2525.
[10] J. Li, X. Liang, D.M. King, Y.-B. Jiang, A.W. Weimer, Appl. Catal. B: Environ. 97 (2010) 220–226.
[11] E. Marceau, X. Carrier, M. Che, O. Clause, C. Marcilly, in: G. Ertl, H. Knözinger, F. Schuth, J. Weitkamp (Eds.), Handbook of Heterogeneous Catalysis, Wiley-VCH, Weinheim, 2008, pp. 467–483.
[12] S. Haukka, T. Suntola, Int. Sci. 5 (1997) 119–128.
[13] B. Delmon, in: G. Ertl, H. Knözinger, F. Schuth, J. Weitkamp (Eds.), Handbook of Heterogeneous Catalysis, Wiley-VCH, Weinheim, 2008, pp. 655–699.
[14] L. Niinistö, M. Ritala, M. Leskelä, Mater. Sci. Eng. B 41 (1996) 23–29.
[15] X. Zhao, M. Yin, M. Liang, L. Liang, C. Liu, J. Liao, T. Lu, W. Xing, Energy Environ. Sci. 4 (2011) 2736–2753.
[16] A. Gewirth, M. Thorum, Inorg. Chem. 49 (2010) 3557–3566.
[17] H. Liu, C. Songa, L. Zhang, J. Zhang, H. Wang, D.P. Wilkinson, J. Power Sources 155 (2006) 95–110.
[18] J. Solla-Gullón, F.J. Vidal-Iglesias, A. López-Cudero, E. Garnier, J.M. Feliu, A. Aldaz, Phys. Chem. Chem. Phys. 10 (2008) 3689–3698.
[19] S. Lai, N. Lebedeva, T. Housmans, M. Koper, Top. Catal. 46 (2007) 320–333.
[20] S. Park, Y. Xie, M.J. Weaver, Langmuir 18 (2002) 5792–5798.
[21] C. Lamy, E. Belgsir, J. Léger, J. Appl. Electrochem. 31 (2001) 799–809.
[22] H.S. Wang, L. Alden, F.J. DiSalvo, H.D. Abruna, Phys. Chem. Chem. Phys. 10 (2008) 3739–3751.
[23] L. Gao, H.L. Huang, C. Korzeniewski, Electrochim. Acta 49 (2004) 1281–1287.
[24] J.S. Spendelowa, A. Wieckowski, Phys. Chem. Chem. Phys. 9 (2007) 2654–2675.
[25] J. Zeng, J. Yang Lee, Int. J. Hydrogen Energy 32 (2007) 4389–4396.
[26] V. Stamenkovic, B. Mun, M. Arenz, K. Mayrhofer, C. Lucas, G. Wang, P.N. Ross, N. Markovic, Nat. Mater. 6 (2007) 241–247.
[27] P. Strasser, S. Koh, T. Anniyev, J. Greeley, K. More, C. Yu, Z. i Liu, S. Kaya, D. Nordlund, H. Ogasawara, M. Toney, A. Nilsson, Nat. Chem. 2 (2010) 454–460.
[28] M. Min, J. Cho, K. Cho, H. Kim, Electrochim. Acta 45 (2000) 4211–4217.
[29] S. Mukerjee, S. Srinivasan, M. Soriaga, J. McBreen, J. Electrochem. Soc. 142 (1995) 1409–1422.
[30] E. Antolini, J. Salgado, E. Gonzalez, J. Power Sources 160 (2006) 957–968.
[31] X. Li, H. Colon-Mercado, G. Wu, J. Lee, B. Popov, Electrochem. Solid State Lett. 10 (2007) B201–B205.
[32] D. Wang, H.L. Xin, R. Hovden, H. Wang, Y. Yu, D. Muller, F. DiSalvo, H. Abruña, Nat. Mater. 12 (2013) 81–87.
[33] G. Bergeret, P. Gallezot, in: G. Ertl, H. Knözinger, F. Schuth, J. Weitkamp (Eds.), Handbook of Heterogeneous Catalysis, Wiley-VCH, Weinheim, 2008, pp. 738–765.
[34] J. Scholten, A. Pijpers, M. Hustings, Catal. Rev. Sci. Eng. 27 (1985) 151–206.
[35] J. Solla-Gullón, E. Gómez, E. Vallés, A. Aldaz, J.M. Feliu, J. Nanopart. Res. 12 (2010) 1149–1159.
[36] D. Frost, C. Mcdowell, I. Woolsey, Chem. Phys. Lett. 17 (1972) 320–323.
[37] A. Santasalo-Aarnio, S. Tuomi, K. Jalkanen, K. Kontturi, T. Kallio, Electrochim. Acta 87 (2013) 730–738.
[38] S. Chumillas, C. Busó-Rogero, J. Solla-Gullón, F.J. Vidal-Iglesias, E. Herrero, J.M. Feliu, Electrochem. Commun. 13 (2011) 1194–1197.
[39] M. Figueiredo, F.J. Vidal-Iglesias, J. Solla-Gullón, V. Climent, J.M. Feliu, Z. Physik. Chem. 226 (2012) 901–917.
[40] F. Maillard, E.R. Savinova, U. Stimming, J. Electroanal. Chem. 599 (2007) 221–232.
[41] J. Solla-Gullón, F. Vidal-Iglesias, E. Herrero, J. Feliu, A. Aldaz, Electrochem. Commun. 8 (2006) 189–194.
[42] J. Xu, X. Liu, Y. Chen, Y. Zhou, T. Lu, Y. Tang, J. Mater. Chem. 22 (2012) 23659–23667.
[43] H. Zhao, J. Dong, S. Xing, Y. Li, J. Shen, J. Xu, J. Hydrogen Energy 36 (2011) 9551–9561.
[44] S. Mentus, Electrochim. Acta 50 (2004) 27–32.
[45] V. Sethuramana, J. Weidnera, A. Haugb, M. Pembertonb, L. Protsailo, Electrochim. Acta 54 (2009) 5571–5582.
[46] M. Campos, W. Siriwatcharapiboon, R. Potter, S. Horswell, Catal. Today 202 (2013) 135–143.
[47] K. Oura, V.G. Lifshits, A.A. Saranin, A.V. Zotov, M. Katayama, Surface Science: An Introduction, Springer, Berlin, 2003, pp. 357–388.
[48] Y. Zhou, D.M. King, X. Liang, J. Li, A.W. Weimer, Appl. Catal. B: Environ. 101 (2010) 54–60.
[49] N. Lakshmi, N. Rajalakshmi, K.S. Dhathathreyan, J. Phys. D: Appl. Phys. 39 (2006) 2785–2790.
[50] P. Hernández-Fernández, S. Rojas, P. Ocón, J.L.G. de la Fuente, P. Terreros, M.A. Penã, J.L. García-Fierro, Appl. Catal. B: Environ. 77 (2007) 19–28.
[51] B. Hammer, J. Nørskov, Surf. Sci. 343 (1995) 211–220.
[52] M. Mavrikakis, B. Hammer, J.K. Nørskov, Phys. Rev. Lett. 81 (1998) 2819–2822.
[53] F. Lima, J. Zhang, M. Shao, K. Sasaki, M. Vukmirovic, E. Ticianelli, R. Adzic, J. Phys. Chem. C 111 (2007) 404–410.
[54] V. Climent, N. García-Araez, J.M. Feliu, in: M.T.M. Koper (Ed.), Fuel Cells Catalysis: A Surface Science Approach, John Wiley & Sons, Inc., New Jersey, 2009, pp. 209–244.
[55] X. Zhang, K.Y. Tsang, K.Y. Chan, J. Electroanal. Chem. 573 (2004) 1–9.
[56] M. Shao, A. Peles, K. Shoemaker, Nano Lett. 11 (2011) 3714–3719.